Liu, Wenqian; Markert, Frank; Hostikka, Simo; Giuliani, Luisa

Thermal responses of a concrete slab under hydrogen fuel cell vehicle fires in a semi-open car park

Published in:
International Journal of Hydrogen Energy

DOI:
10.1016/j.ijhydene.2024.06.096

Published: 04/07/2024

International Journal of Hydrogen Energy 73 (2024) 800–811

Contents lists available at ScienceDirect

International Journal of Hydrogen Energy

journal homepage: www.elsevier.com/locate/he

Thermal responses of a concrete slab under hydrogen fuel cell vehicle fires in a semi-open car park

Wenqian Liu[a,*], Frank Markert[a], Simo Hostikka[b], Luisa Giuliani[a]

[a] Department of Civil and Mechanical Engineering, Technical University of Denmark, Brovej 118, Kgs, Lyngby, 2800, Denmark

[b] Department of Civil Engineering, Aalto University, Rakentajanaukio 4 A, Espoo, 02150, Finland

ARTICLE INFO

Handling Editor: Shohji Tsushima

Keywords:
Hydrogen fuel cell vehicle
Localized fire
Concrete car park
Coupling methodology
Thermal response

ABSTRACT

This work aims to investigate the thermal behaviors of the concrete ceiling slab of a semi-open car park exposed to localized fire in hydrogen fuel cell vehicles. For this purpose, a numerical simulation of the hydrogen fuel cell vehicle fire was performed in the Fluid Dynamic Simulator and then coupled with a subsequent thermal analysis of concrete structure carried out in ANSYS Mechanical APDL. In particular, an automatic procedure was used to extract the output of the fire simulation and apply them as boundary conditions of the thermal model. The one-way coupling procedure involving fire simulation and transient thermal analysis has been validated by comparing it with concrete temperatures of a previous test study. Then, two parameters, the diameter of thermal pressure relief devices (1 mm, 2 mm, 3 mm, and 4 mm) and fire spread time between vehicles (0 min, 20 min, and 30 min), are taken into account to study the thermal properties of concrete. The analysis revealed that an increase in the nozzle diameter of the thermal pressure relief device leads to a rise in the maximum concrete surface temperature. The simulation results also showed that the maximum value of the heat release rate increases with a higher value of the nozzle diameter of the thermal pressure relief device and a shorter fire spread time between vehicles.

1. Introduction

Abbreviations			
HFCV	Hydrogen fuel cell vehicles	ξ	Ratio of degraded concrete strength to the nominal strength at the ambient temperature
FDS	Fluid Dynamic Simulator	q''_{tot}	Total heat flux
TPRD	Thermal pressure relief devices	q''_{rad}	Heat flux exchanged by radiation
HRR	Heat release rate	q''_{conv}	Heat flux exchanged by convection
CFD	Computational Fluid Dynamics	$q''_{r,inc}$	Radiative incident thermal energy
FEA	Finite Element Analysis	T_w	Surface temperature
FTMI	Fire-Thermomechanical Interface	ε	Absorptivity of the radiation or Emissivity of the radiation
AST	Adiabatic Surface Temperature	T_g	Gas temperature
NIST	National Institute of Standards and Technology	h_g	Convective heat transfer surface coefficient
FVM	Finite Volume Method	$q''_{tot,CFD}$	Total heat flux obtained in CFD
LES	Large Eddy Simulation	σ	Stefan-Boltzmann constant
Nomenclature		$q''_{r,inc,CFD}$	Radiative incident thermal energy in CFD
$T_{g,CFD}$	Gas temperature in CFD	T_{AST}	Adiabatic surface temperature
$T_{w,FE}$	Surface temperature in FEA	[C]	Specific heat matrix
[K]	Conductivity matrix	{T}	Vector of nodal temperature
$\{\dot{T}\}$	Time rate of the nodal temperature	{Q}	Global nodal heat flow

Car park fires have gained increasing attention because modern vehicle fires have recently become more severe and frequent than in the past. Modern vehicles not only have more combustible materials, like plastics but also make more frequent use of alternative energy, such as

* Corresponding author.
E-mail addresses: weliu@dtu.dk (W. Liu), fram@dtu.dk (F. Markert), simo.hostikka@aalto.fi (S. Hostikka), lugi@dtu.dk (L. Giuliani).

https://doi.org/10.1016/j.ijhydene.2024.06.096
Received 5 March 2024; Received in revised form 1 June 2024; Accepted 8 June 2024
Available online 13 June 2024

electric batteries and hydrogen fuel cells, which may lead to new fire scenarios [1]. For example, a fire at the Luton airport car park, triggered by a vehicle fault, resulted in damage to over 1500 vehicles [2]. In another case, the Felicity Ace car carrier caught fire [3] and burned thousands of vehicles, which is suspected the intensity of the blaze is attributed to the electrical vehicles. Similarly, the Fremantle Highway car carrier fire [4] destroyed or damaged as many as 2800 vehicles. According to these cases, a car park fire is likely to spread to several vehicles and may lead to thousands of vehicles damaged and structural collapse. To reduce the economic losses and the influence of a car park fire on the structural elements of a car park, it is necessary to study the fire behaviors of modern vehicle fires in a car park.

Vehicle bodies and fuel systems are the two main parts of a vehicle. Owing to the similar material used in modern vehicles, the major discrepancy among modern vehicle fires is caused by the fuel. For instance, the hydrogen fuel cell vehicle (HFCV) stores the hydrogen gas fuel in a high-pressure tank with a special device called a "Thermal Pressure Relief Device" (TPRD). The hydrogen gas can be released from storage tanks through a TPRD nozzle in a fire accident and may generate high-velocity jet fire flames [5], affecting the fire size and fire spread time in a car park. In terms of these special characteristics of HFCV fires, the HFCV fires will be investigated in this study, to provide more information about modern vehicle fires in a car park.

In a car park fire, heating from burning vehicles can affect the adjacent structures, e.g., beams, columns, and slabs. Structures suffering an intensive fire could lose stability or part of their load capacity. However, the temperature distribution of structures in a car park fire is associated with the location and time of the fire onset and spread, so it is difficult to rely on the use of simplified design methods for designing a car park against these fire scenarios [6–8]. In order to obtain a realistic temperature field of the structure, Computational Fluid Dynamics (CFD) simulation of the different car fire scenarios can be performed. The solid phase involving the thermal properties of structures is simulated in Finite Element Analysis (FEA) software due to limitations in solving the solid phase heat transfer in CFD software. The use of two separate software, however, makes such analyses quite demanding, particularly in the case of a manual transfer of data between the CFD and FEA software. Therefore, a specialized tool capable of connecting the CFD model and the FEA model is extremely useful in studying the thermal response of structures under particular fire scenarios.

However, the information transfer from a CFD model to an FEA model is challenging, because of the difference in the spatial discretization, the time scale, and even the software codes [9,10]. To implement the connection between CFD and FEA, Prasad and Baum [11] proposed a methodology to combine the FDS and ANSYS parametric design language, in which only the radiative heat transfer is taken into account in the heat transfer between the fire and structures. Tondini et al. [12] developed an interface that can connect FDS and SAFIR, including both convection and radiation heat transfer. Silva et al. [13] introduced an interface model called Fire-Thermomechnical Interface (FTMI), which transfers heat results from convection and radiation from FDS to ANSYS. In particular, the Adiabatic Surface Temperature (AST) concept propounded by Wickstrom [14] was used in this FTMI, showing an efficient method of transferring the output information of FDS to the ANSYS model [15].

Coupled CFD-FEA methods are broadly applied for analyzing structural response under complex fire scenarios. For example, Alos-Moya et al. [16] investigated the fire response of steel girder composite bridges with a length of 115.2 m. Silva et al. [17] proposed a coupling procedure concerning FDS and ANSYS, applying this coupling method to estimate the thermal-mechanical properties of a nuclear cylindrical steel containment vessel that suffered an accidental external fire condition. Tondini et al. [18] studied the structural behaviors of a multi-story steel-concrete composite open car park under simplified localized fire using FDS-SAFIR integrated methodology. In addition, Yan et al. [19] also employed the FDS-SAFIR interface method to analyze the temperature of a steel open car park under a fire scenario. According to these studies, CFD-FEA coupling is a vital way to investigate the structural behaviors under a real fire scenario, especially for these large structures and complex fire scenarios.

Two common approaches are used for combining CFD and FEA simulations, namely one-way coupling and two-way coupling [20]. In the one-way coupling method, the fire model in CFD is calculated independently of the thermal response in FEA, only based on the pre-defined boundary conditions [21]. In contrast, the influence of the structural consequence on the fire model is considered in the two-way coupling approach [15]. Compared with the one-way coupling method, the two-way coupling approach can present the fire scenario more realistically but several limitations are still in the application, such as complex calculation methods, and high cost [20].

In general, the fire performances of structures exposed to HFCV fire are still a relatively new subject, and it only rarely reported. To bridge this deficiency, this study aims to employ a one-way coupling way to analyze the thermal response of the concrete structures under HFCV fires in a semi-open car park. Particularly, distinct HFCV fire scenarios including different TPRD diameters (1 mm, 2 mm, 3 mm, and 4 mm) and fire spread times (0min, 20min, and 30min) between HFCVs are taken into consideration. In light of these CFD-FEA coupling analyses, some guidance relevant to the fire safety assessment of the concrete structures will be provided for fire engineers.

2. Methodology

2.1. CFD model

FDS is an open-source program that is widely used to study building fires for fire engineers. It was developed by the National Institute of Standards and Technology (NIST), with the aim of solving the Navier-Stokes equations numerically for the low-mach-driven fluid flow [22,23]. A simple chemistry model was used in the FDS simulation. The grey gas model with the Finite Volume Method (FVM) was employed to simulate the thermal radiation. Turbulence was simulated using the Large Eddy Simulation (LES) approach, while eddy viscosity was modeled by the Deardoff turbulence model. All geometries are approximated as a series of rectangular parallelepipeds in FDS. The heat conductivity calculation in FDS is one dimension. In this study, FDS version 6.7.9 was employed for the fire simulation.

2.2. FDS2FTMI interface

In a fire scenario, heat can be conveyed from flames and hot gases to the surfaces of a structure through radiation and convection [13]. The total heat flux q''_{tot} exchanged by the surface with the surroundings is obtained as a sum of the two components in Eq. (1), i.e. the heat flux exchanged by radiation q''_{rad} and by convection q''_{conv}.

$$q''_{tot} = q''_{rad} + q''_{conv} \tag{1}$$

The radiation heat flux q''_{rad} is the difference between the radiative energy absorbed on the exposed surface (which is a part of the radiative incident thermal energy $q''_{r,inc}$) and the radiative energy emitted by the surfaces (which depends on the surface temperature T_w). Since the absorptivity and emissivity of the radiation are identical, on the basis of Kirchhoff's law, they can both be indicated with the same symbol ε. The convection heat flux q''_{conv} is proportional to the difference between the gas temperature T_g and the structural surface temperature T_w by means of the convective heat transfer surface coefficient h_g, following the approximation of Newton's law of cooling. Hence, the total heat flux obtained in CFD $q''_{tot,CFD}$ can be reorganized as Eq. (2).

$$q''_{tot,CFD} = \varepsilon\left(q''_{r,inc} - \sigma T_w^4\right) + h_g\left(T_g - T_w\right) \tag{2}$$

The structural surface temperature T_w obtained in the FDS model is inaccurate owing to the limitation of the solid-phase heat transfer calculation in FDS [8,22]. Instead, the FEA solver can simulate the heat transfer in the solid phase precisely by imposing necessary thermal boundaries, such as $T_{w,FE}$ or net heat flux. From an FEA viewpoint, the total heat flux is expressed as Eq. (3) [8,24].

$$q''_{tot,FE} = \varepsilon\left(q''_{r,inc,CFD} - \sigma T^4_{w,FE}\right) + h_g\left(T_{g,CFD} - T_{w,FE}\right) \tag{3}$$

where σ is the Stefan-Boltzmann constant $5.6703 \times 10^{-8}\mathrm{W}/\left(\mathrm{m}^2\mathrm{K}^4\right)$.

However, the $q''_{r,inc,CFD}$ and $T_{g,CFD}$ are not possible to calculate in the FEA solver. Hence, it is necessary to build an interface to connect CFD and FEA models. To accomplish this, the adiabatic surface temperature (AST) T_{AST}, which takes into account a virtual, perfectly insulated object in place of a real solid exposed to heating, was introduced to calculate the total heat flux [23,24]. In the AST method, the adiabatic virtual surface is in thermal equilibrium with its surroundings, and the total heat flux exchanged with the surface is therefore zero, as shown in Eq. (4). The temperature of this adiabatic virtual surface T_{AST} can be obtained as output from the fire simulation in FDS. Based on Eq. (3) and Eq. (4), an accurate surface temperature $T_{w,FE}$ can be calculated at each time step of the thermal analysis in the FEA model, as shown in Eq. (5).

$$q''_{tot,CFD} = \varepsilon\left(q''_{r,inc,CFD} - \sigma T^4_{AST}\right) + h_g\left(T_{g,CFD} - T_{AST}\right) = 0 \tag{4}$$

$$q''_{tot} = \varepsilon\sigma\left(T^4_{AST} - T^4_{w,FE}\right) + h_g\left(T_{AST} - T_{w,FE}\right) \tag{5}$$

The approach linking CFD and FEA models is determined by discretization methods in two models, e.g., mesh size, and element shape. For example, an FDS domain is always discretized into hexahedrons, while a thermal model in ANSYS allows for discretization into various elements, including hexahedrons and 3D planes [13]. To realize the data transfer between CFD and FEA models, the results in the fire model need to be mapped to the structural model in the FEA solver. Hence, a one-way coupling interface between FDS and ANSYS Mechanical APDL called FDS2FTMI was developed to automatically transmit FDS results to ANSYS by Silva [25].

The mapping in the FDS2FTMI is based on the extra node localized at the center of each element on the structural exposed surfaces, as shown in Fig. 1. The position and number of extra nodes are determined by the mesh generated in the FEA model. FDS2FTMI can search the exposed surfaces in ANSYS and collect information on extra nodes, such as corresponding normal directions, positions et al. After that, FDS2FTMI obtains the correct thermal boundary parameters (convection heat transfer coefficient h_g and adiabatic surface temperature T_{AST}) of exposed surfaces in the boundary file (.bf) in FDS [13], and imposes these boundary conditions on the FEA model. In brief, the coupling procedure is achieved by mapping the FDS and ANSYS models and transferring the data automatically from one another.

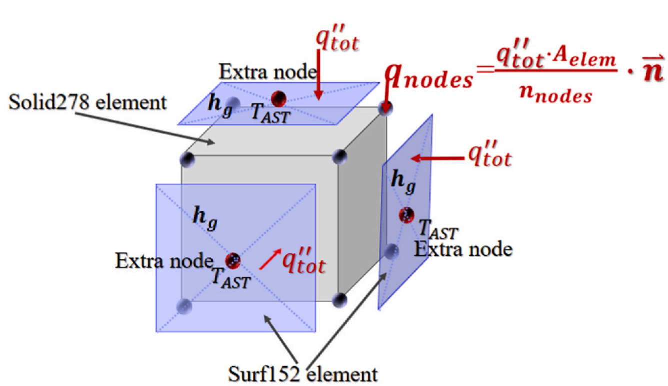

Fig. 1. FDS2FTMI interface tool application process.

2.3. FEA model

The Full solution method with the Newmark algorithm is used for the transient thermal analysis in ANSYS to study the thermal properties of structures [26]. In the FE model, different elements are used for distinct materials to discretize the FE model in thermal analysis [27]. As for the concrete reinforcement (RC) structures, REINF264 (2-node element) is employed to simulate the heat transfer in the steel reinforcement, and SOLID278 (8-node element) is used for concrete.

Thermal boundaries of structures, such as heat flux or surface temperature, are required to be prescribed in the FEA model [28]. When it refers to CFD-FEA coupling, these thermal boundaries obtained from FDS can be automatically prescribed to the SURF152 element (4-node element) in ANSYS using FDS2FTMI, as shown in Fig. 1. T_{AST} is prescribed at the extra node on the element SURF152, and h_g is imposed on the surface of element SURF152.

In the FEA model, the heat transfer in solid structures is mainly controlled by thermal conduction, and the governing equation of thermal analysis in ANSYS can be expressed as Eq. (6).

$$[C]\{\dot{T}\} + [K]\{T\} = \{Q\} \tag{6}$$

where $[C]$ is the specific heat matrix, $[K]$ is the conductivity matrix, $\{T\}$ is the vector of nodal temperature, $\{\dot{T}\}$ is the time rate of the nodal temperature, $\{Q\}$ is the global nodal heat flow.

In Eq. (6), the thermal conductivity and specific heat vary with the temperature of the material. In this study, the temperature variation of such thermal properties (specific heat and thermal conductivity) is adopted from Eurocodes [29,30]. Concrete density and steel density are $2400\ \mathrm{kg/m^3}$ and $7850\ \mathrm{kg/m^3}$. Additionally, the resultant emissivities for concrete and steel are prescribed as 0.85 and 0.7, respectively.

3. Validation of the coupling process

To validate the FDS and ANSYS coupling process, the temperatures of numerical predictions are compared with test results in the literature [31]. In the test, an RC beam without protection was exposed to an ASTM E119 fire in a propane furnace. The test facilities consist of a rectangular furnace with dimensions of $3.05\ \mathrm{m} \times 2.44\ \mathrm{m} \times 1.68\ \mathrm{m}$ (length $\times$width $\times$ height) and an RC beam with dimensions of $3.96\ \mathrm{m} \times 0.254\ \mathrm{m} \times 0.408\ \mathrm{m}$ (length $\times$ width $\times$ height). Hence, three external surfaces of an RC beam segment were exposed to the furnace fire, as shown in Fig. 2(a).

The FDS model of an RC beam subjected to fire is present in Fig. 2(b). In this FDS model, the fire source generated by the propane combustion is simulated by specified solid surface temperatures on the internal walls of the furnace. One reason for this method is that propane burners in the furnace were used to create the standard ASTM E119 fire scenario; another is the unknown information on propane burners. The mesh size of this FDS model is 0.1 m. AST and h_g are recorded in the boundary file of the output results.

The FEA model of this RC beam has the same geometry and coordinate system as the CFD model, as displayed in Fig. 2(c). The difference is that steel reinforcements are considered in an FEA model while ignored in an FDS model. This is because AST and h_g are mainly influenced by the fire source. In addition, the simplification of an FDS model to some extent could reduce the complexity of the simulation. Five longitudinal reinforcements are arranged in this beam, two rebars with a diameter of 13 mm are in the compression zone, and three with a diameter of 19 mm are in the tension zone. In addition, 6 mm stirrups are placed in the beam with a spacing of 150 mm. For the sake of detecting the temperature of concrete, two thermocouples are mounted inside the concrete beam, and one thermocouple is set on the bottom surface of the beam. The grid size of this FEA model is smaller than in the FDS model, which is 0.04 m.

After calculation, the nodal temperature on the beam section is

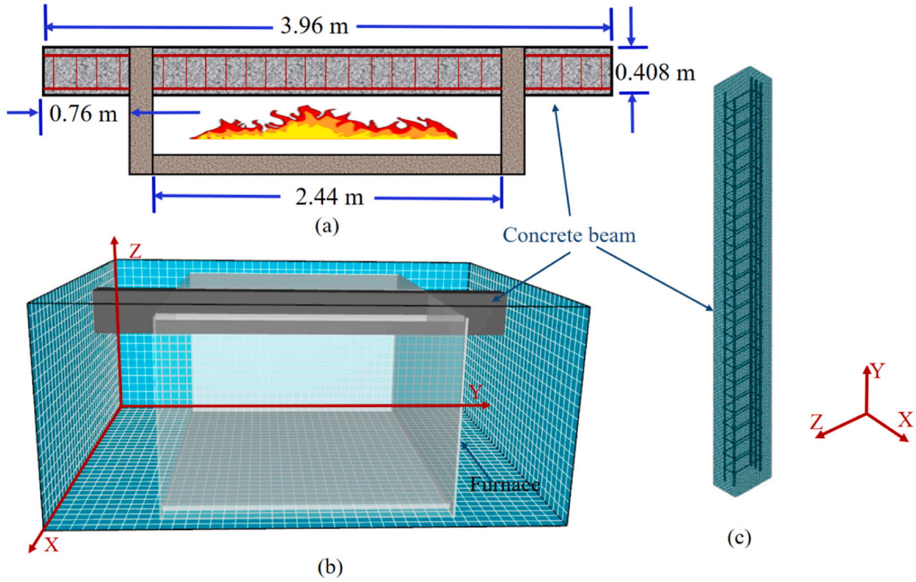

Fig. 2. Sketch of an RC beam: (a) Beam exposed to fire, (b) Beam model in FDS, (c) Beam model in ANSYS.

shown in Fig. 3. 'TC0' refers to the concrete temperature on the beam surface, and 'TC1' and 'TC2' are the concrete temperatures inside the beam. Fig. 3 indicates a good agreement between the test and predicted concrete temperature in ANSYS. In particular, the calculated concrete temperatures of these three devices are overall lower than those registered in the test. However, the differences between the test and simulation temperatures decrease with time and a quite good agreement between the predicted and measured temperatures can be seen after 100–120 min of fire exposure. The differences may be attributed to the temperature curves applied in the FDS model being slightly different from the curve attained in real propane combustion. Additionally, material models of concrete and steel prescribed in an FEA model have some discrepancies with respect to the real materials.

4. Numerical model of the car park

As mentioned in the introduction, the influences of HFCV fires under different TPRD nozzle diameters and fire spread times on a concrete TT slab ceiling are studied for a fire scenario based on a semi-open car park located in Copenhagen [32]. This concrete car park has a dimension of 119.4 m × 17.5 m × 3.2 m (length × width × height), depicted in Fig. 4 (a). The distance between two adjacent webs of a TT slab is 1.2 m. The height of the web and flange of this TT slab is 0.6 m and 0.2 m, respectively.

The FDS domain only considers a part of the car park, specifically a floor area of 8.5 m by 8 m, as visible in Fig. 4(b). The reduction of the domain is meant to limit the computational cost for the whole car park simulation and is justified by the limited influences of the remaining area on the local development of the HFCV fire temperatures below the slab. In this FDS model, the ceiling and floor are simulated as concrete with constant material properties. Instead, all four vertical sides of the modeled car park segment are considered openings.

The HFCV fire is assumed to consist of vehicle body fire and hydrogen jet fire here. To present these in FDS, the HFCV is modeled by an adiabatic block with a 4.7 m length, 1.9 m width, and 0.75 m height based on the size of the Hyundai Nexo hydrogen fuel cell SUV [33]. The fire due to the burning vehicle main body is modeled by assigning the heat release rate (HRR) of the Hyundai Nexo combustion test [34] to the

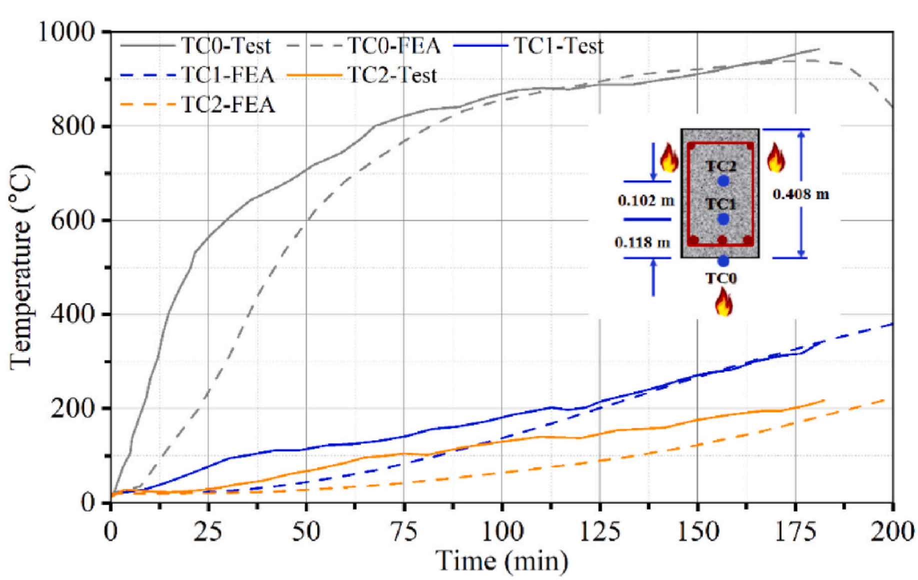

Fig. 3. Comparison of concrete temperature in Test (after [32])and FEA model.

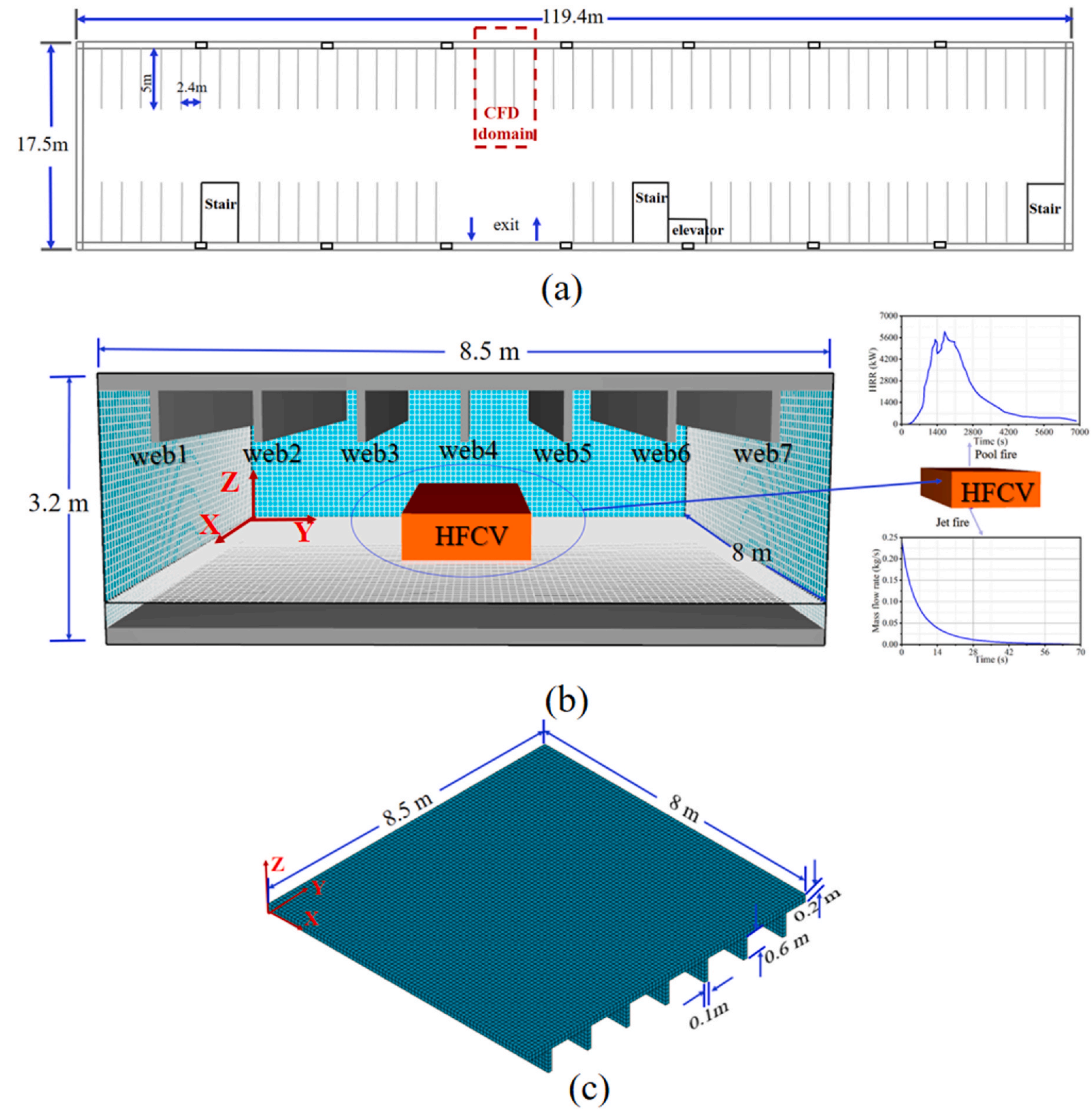

Fig. 4. Car park: (a) Layout of a car park in Copenhagen after [32], (b) Car park model in FDS, (c) Ceiling of a car park slab model in ANSYS.

top surface of the block representing the car. The jet fire instead is modeled by means of three virtual nozzles placed on the bottom surface of the block at a distance of 0.25 m to the floor in accordance with the position of the three hydrogen tanks of the Hyundai Nexo. The hydrogen mass flow rate prescribed in this jet fire model is calculated by e.laboratory [35] in terms of values of tank pressure, tank volume, and TPRD nozzle diameter. Detailed information on this model and justification for the use of a low-Mach number formulation used in FDS to simulate the hydrogen jet fire can be found in a previous paper published by the authors [36].

Due to the fine resolution required in the jet fire model, two computational meshes are prescribed in this car park fire model. The one including jet fire models has a mesh size of 0.05 m, and the other is 0.1 m, resulting in a total of 455600 cells. The car park is naturally ventilated and the initial air condition is assumed still. As a result of the fire, the ventilation is through the opening as thermal flows develop, causing the hot gases to leave the car park through the upper side. Therefore, the thermal behaviors of the ceiling in this car park are of great interest to investigate. The FEA model of the ceiling is exhibited in Fig. 4(c) with a constant mesh size of 0.05 m. An implicit thermal analysis has been conducted in ANSYS, based on Newton Raphson method and backward Euler time integration with a time step of 20 s.

To obtain reliable simulation results, the validation of this car park model can be divided into three key components: the HFCV fire model in FDS, the CFD-FEA coupling process, and the concrete structure thermal model in ANSYS. The HFCV fire model can be validated by simulating the HFCV main body fire using HRR curves from an existing test [34], and by incorporating a hydrogen jet fire model [36]. The validation for the coupling process, as well as the concrete structure thermal model in ANSYS, is detailed in section 3.

A total of seven vehicle fire scenarios involving four TPRD nozzle diameters (1 mm, 2 mm, 3 mm, and 4 mm) and three fire spread times (0 min, 20 min, and 30 min) from a middle HFCV to two adjacent HFCVs are considered in this study to investigate the thermal behaviors of the concrete ceiling in the semi-open car park, as shown in Table 1. Initial mass flow rates and hydrogen blowdown durations are calculated by e-laboratory [35]. In the fire spread scenarios, the distance between two adjacent HFCVs is 0.5 m [32,37]. The TPRD active time is 18 min after

Table 1
Details of numerical simulations.

Scenario No.	TPRD nozzle diameter (mm)	Initial mass flow rate (kg/s)	Fire spread time (min)	Car no.	Hydrogen blowdown duration(s)
1	1	0.0268	–	1	665.6
2	2	0.1072	–	1	160.0
3	3	0.2412	–	1	67.2
4	4	0.4289	–	1	35.2
5	2	0.1072	0	3	160.0
6	2	0.1072	20	3	160.0
7	2	0.1072	30	3	160.0

the vehicle body fire [34], meaning that the jet fire starts after the HFCV body fire at 18 min in this HFCV fire model. The fire spread time refers to the time interval between two vehicle body fires, and the TPRD active time is still after 18 min of the corresponding vehicle body fire.

In fire scenarios 1–4, only a single vehicle is implicated in the car park fire. However, in scenarios 5–7, the fire involves three vehicles. A larger segment of the slab, which includes 7 webs (labeled as "web1" to "web7" and the pertinent flange is considered for the analysis of these scenarios. For all fire scenarios, measurement points were in a specific section of the ceiling slab, namely only the web labeled as "web4 in Fig. 4, along with the pertinent flanges on both the right and left sides, as depicted in Fig. 5. Here, 'h' represents the depth of the concrete.

To estimate the concrete strength (residual compressive strength and compressive strength), Herz's degradation model [38] shown in Eq. (7) can be used, where ξ represents the ratio of degraded concrete strength at high temperature to the nominal strength at the ambient temperature:

$$\xi(T) = k + \frac{1-k}{1 + \left(\frac{T}{T_1}\right) + \left(\frac{T}{T_2}\right)^2 + \left(\frac{T}{T_8}\right)^8 + \left(\frac{T}{T_{64}}\right)^{64}} \tag{7}$$

In this equation [38], k, T1, T2, T8, and T64 are constants that depend on the material and on whether the strength at temperature T (during heating, also referred to as "hot condition") or the residual strength after being heated to T and cooled down to 20C are of interest (referred to as "cold condition"). In particular, for calcareous concrete, the slab is made of, the values used for $(k, T_1, T_2, T_8, T_{64})$ are $(0, 1500, 580, 520, 690)$ for the hot condition and $(0, 100000, 100000, 1150, 1150)$ for the residual strength of concrete.

5. Results of different fire scenarios

5.1. Single burning vehicle (scenarios 1 to 4) with different TPRD nozzle diameters

The gas temperature and flame of the car park fire involving a single vehicle at 1122.2 s is displayed in Fig. 6(a). It can be seen that the maximum gas temperature at this time is larger than 900 °C. Figs. 6(b-1)-(b-4) show concrete temperatures of the car park ceiling under different TPRD nozzles at time 2100 s. In Figs. 6(b-1)-(b-4), the maximum concrete temperatures of 1 mm, 2 mm, 3 mm, and 4 mm TPRD nozzle are 748.3 °C, 768.4 °C, 800.5 °C, and 813.9 °C, separately, indicating that the maximum concrete surface temperature increases with the TPRD nozzle diameter. In addition, the concrete maximum surface temperature is 813.9 °C, as expected, lower than the maximum gas temperatures due to the concrete surface resistance to radiation and convection [39]. As for cross-section temperatures of the ceiling, the center concrete temperatures of web4 are always lower than 200 °C at time 2100 s as the TPRD nozzle changed from 1 mm to 4 mm. Moreover, the heat travels into the flange of this TT slab ceiling with a limited depth, almost less than one mesh size (0.05 m) at this time.

Concrete temperature histories under different depths and HRR histories during the HFCV fire are displayed in Fig. 7. The red curves refer to the HRR of this fire, AST curves representing the input environment temperature in the mode are presented by grey curves, and the other curves show concrete temperatures in the same section (X = 3.85 m, Y = 4.25 m) at different depths (with labels '0 m' to '0.8 m'). In comparison to the maximum HRR values in Figs. 7(a)–(d), the maximum HRR value increases with a larger nozzle diameter as the TPRD nozzle diameter varies from 1 mm to 4 mm. For example, the maximum HRR with a value of 20 MW appears as the TPRD nozzle diameter is 4 mm. Furthermore, striking sudden peak points are shown in these four HRR curves, in which the peak HRR is caused by the TPRD activation [40]. Based on Figs. 7(a)–(d), AST curves are not very smooth because of the larger time step of the boundary file in FDS. Regarding concrete temperatures, these concrete temperature curves reach all their peak values at a later time than the AST curves and, as expected, the delay of the peak increases as concrete depth increases. In addition, the disparity of maximum temperature is much higher between the web bottom surface and 0.05 m depth, which is larger than 350 °C.

Fig. 8(a) presents concrete temperatures and ratios of concrete compressive strength at the same section (X = 3.85 m, Y = 4.25 m) at various depths and TPRD nozzle diameters. Note that concrete temperatures in Fig. 8(a) are extracted at the time when concrete temperatures of depth 0.05 m arrive at peak values, and ratios of compressive strength are calculated by Eq. (7) with hot conditions (strength during the fire). In Fig. 8(a), the temperatures of concrete web4 are above

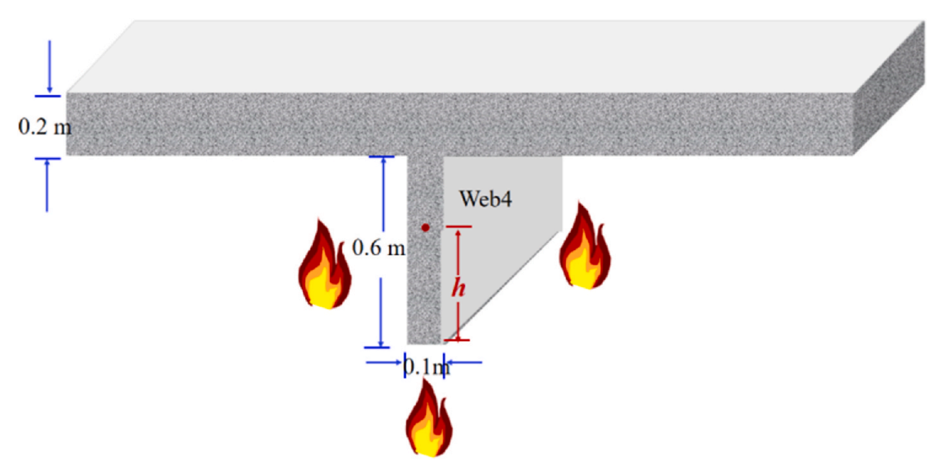

Fig. 5. Measurement points in the FEA model (location of web4 center: Y = 4.25 m).

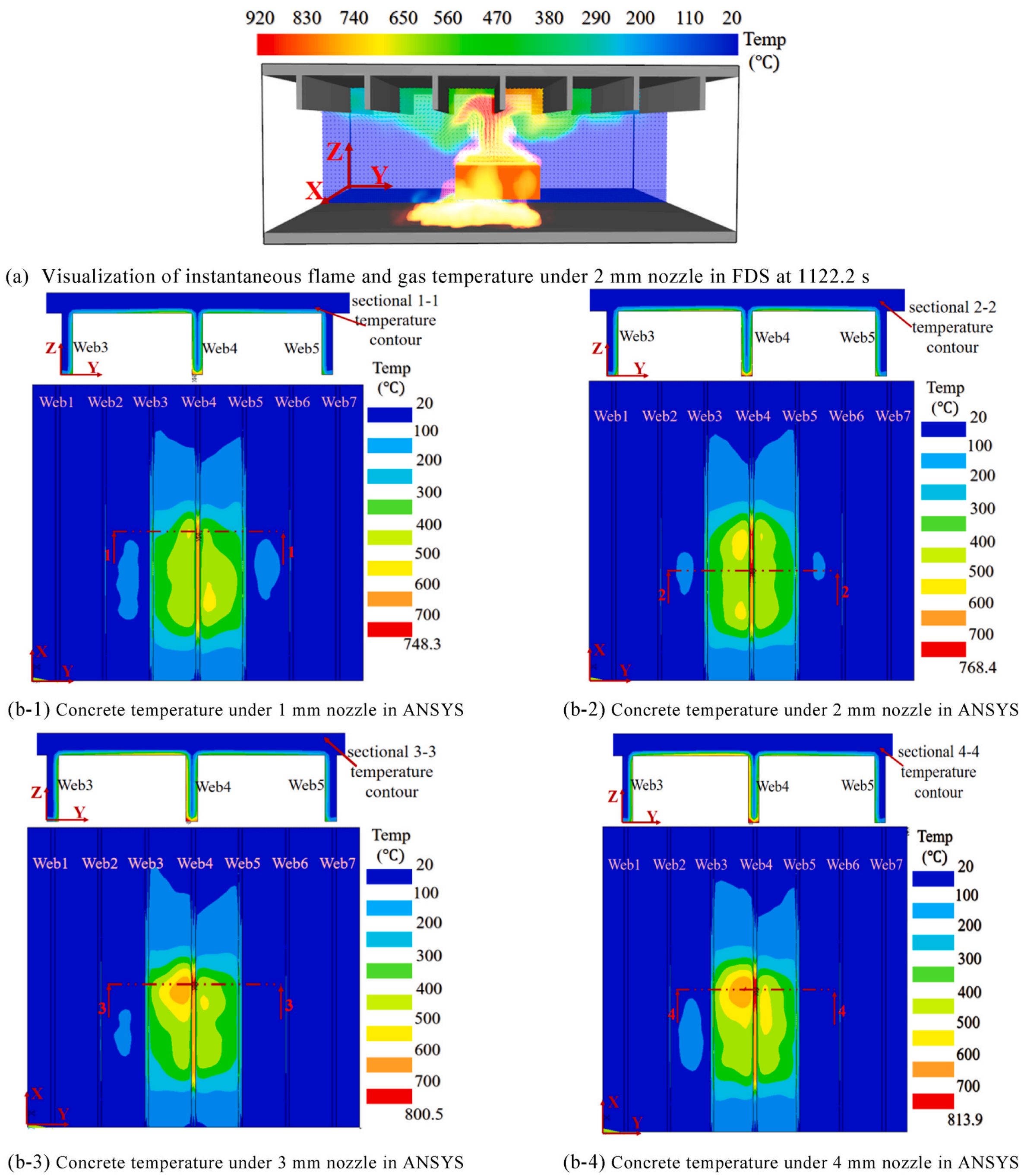

Fig. 6. Visualization of instantaneous flame with gas temperature in FDS at 1122.2 s, and temperature contours of concrete surface and ceiling cross-section in ANSYS under different TPRD nozzles at 2100 s.

200 °C, and concrete temperatures vary greatly near the junction of the flange and web. The concrete compressive strength at this ceiling cross-section decreases to 0.81–0.96 times the normal compressive strength. Moreover, the TPRD nozzle diameters play an important role in the concrete compressive strength of web4, where the concrete compressive strength decreases with a rise in nozzle diameter.

Fig. 8(b) shows the maximum concrete temperatures and ratios of residual compressive strength at the same section (X = 3.85 m, Y = 4.25 m) at various depths and TPRD nozzle diameters. Different from Fig. 8 (a), the concrete temperatures are from each peak temperature at different depths, and the ratios of residual compressive strength are obtained by Eq. (7) with cold conditions (residual strength). In the same range of depth, the residual compressive strength of web concrete is influenced by the TPRD nozzle diameter, and the larger the TPRD diameter, the lower the residual compressive strength. However, the concrete residual compressive strength changes a lot near the intersection of the flange and web (0.55 m–0.7 m). This is because two sides of the web and the bottom surface of the flange are exposed to fire.

5.2. *Three vehicles (scenarios 5 to 7) with different fire spread time*

The influences of fire scenarios, including three HFCVs with 2 mm TPRD nozzles and different fire spread times on the concrete ceiling, are investigated in this section. The visualization of the gas temperatures and fire flames at 1122.2 s is presented in Fig. 9(a), and the concrete temperatures of the car park ceiling at the peak concrete surface

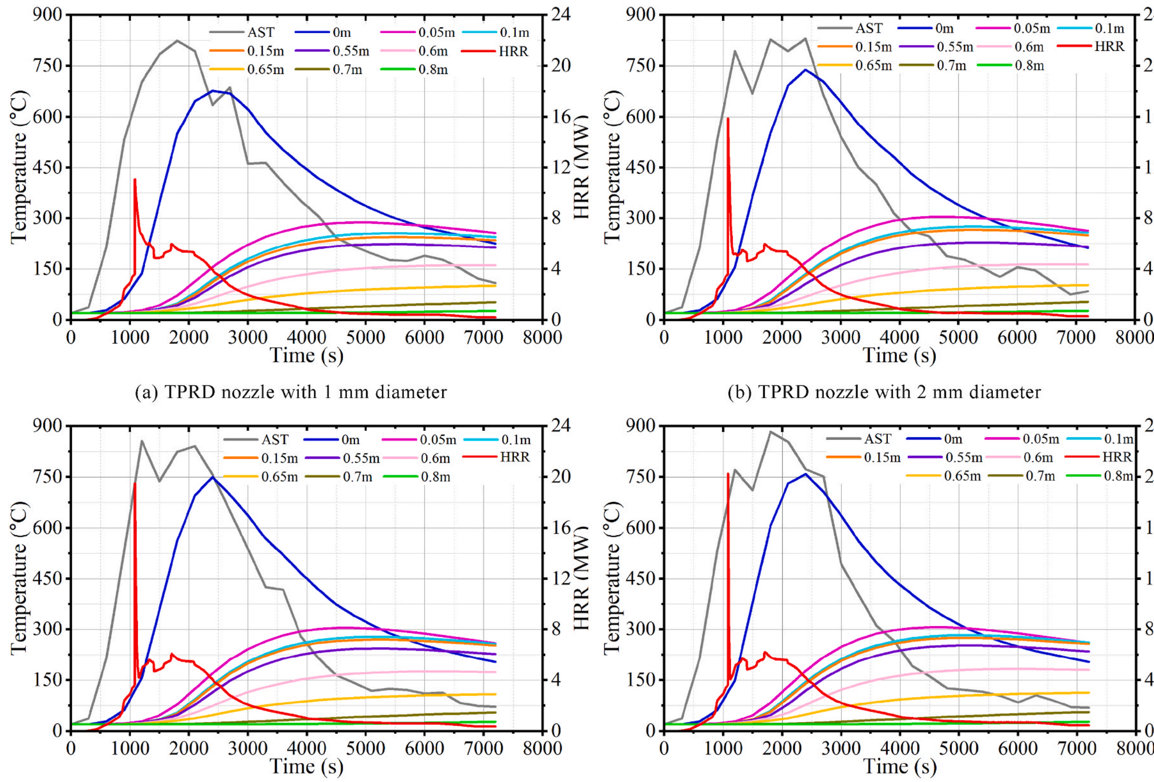

(a) TPRD nozzle with 1 mm diameter (b) TPRD nozzle with 2 mm diameter

(c) TPRD nozzle with 3 mm diameter (d) TPRD nozzle with 4 mm diameter

Fig. 7. Concrete temperature and HRR histories under different TPRD nozzles and concrete depth h varying from 0 to 0.8 m from the bottom beam surface (location of a line extracted data: X = 3.85 m, Y = 4.25 m).

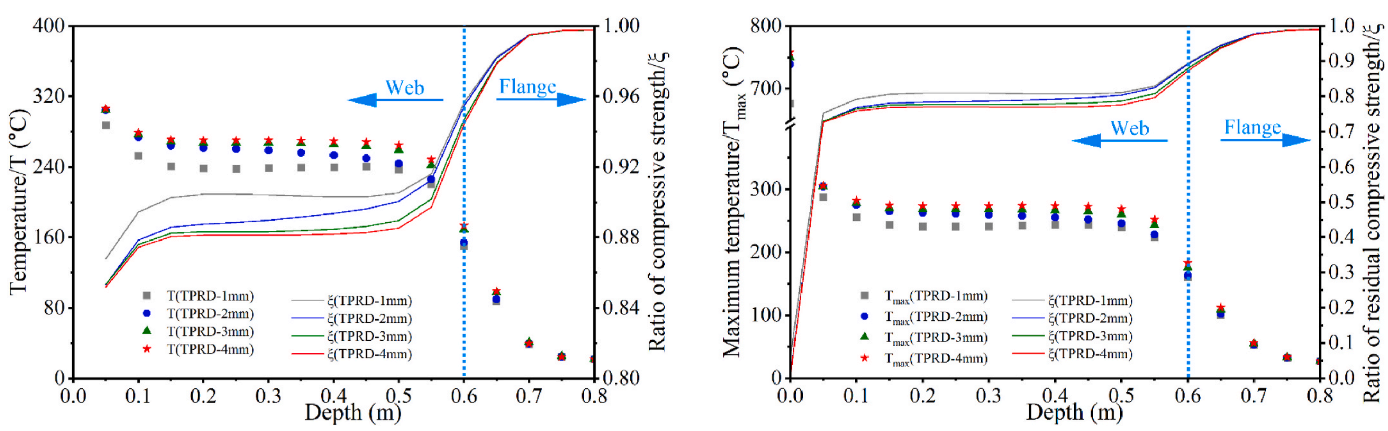

(a) (b)

Fig. 8. Concrete temperatures and ratios of concrete strength in a fire along concrete depth h under different TPRD nozzle diameters (x = 3.85 m, y = 4.25 m): (a) hot condition (b) cold condition.

temperature time are shown in Figs. 9(b-1)-(b-3). In light of Fig. 9(a), the fire flames are concentrated on the bottom of the ceiling and propagate to the ceiling sides. The maximum concrete surface temperature with a value of 871 °C appears on web4 when all three HFCVs start burning at the same time (Fig. 9(b-1)). When the fire spread time between cars is 20 min or 30 min (Figs. 9(b-2) and (b-3)), the maximum concrete surface temperatures are in the web6 with values larger than 800 °C. Additionally, the time at which the maximum concrete surface temperature is registered increases from 2100 s to 3300 s, and to 3900 s as the fire spread between cars increases from 0 min to 20 min, and 30 min, respectively.

The HRR histories and the corresponding concrete temperature histories along a section (X = 3.85 m, Y = 4.25 m) of the ceiling under different fire spread times are shown in Fig. 10. Among these three scenarios, a maximum HRR value of 44 MW appears in Fig. 10(a), involving three HFCVs burning simultaneously. Moreover, the maximum HRR value decreases, when the fire spread time increases and is 40.5 MW for 20 min fire spread time and 39.5 MW for 30 min. The HRR history curves have two obvious peak values in Figs. 10(b) and (c) related to 20 min and 30 min fire spread, respectively. The first crest is attributed to the TPRD activation of the middle HFCV, and the second crest is due to the TPRD activation of two side HFCVs [40]. When it comes to the concrete web temperatures, in all three scenarios 5, 6, and 7 the maximum temperature at a depth h = 0.05 m is larger than 320 °C,

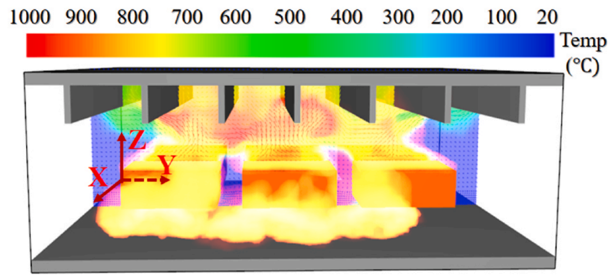

(a) Visualization of instantaneous flame with vector of gas temperature in FDS at 1122.2s in scenario 5 (three HFCVs start burning at the same time)

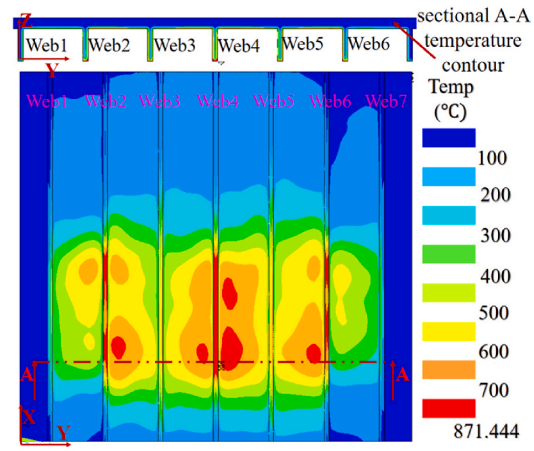

(b-1) Concrete temperature in ANSYS at 2100s in scenario 5 (three HFCVs start burning at the same time)

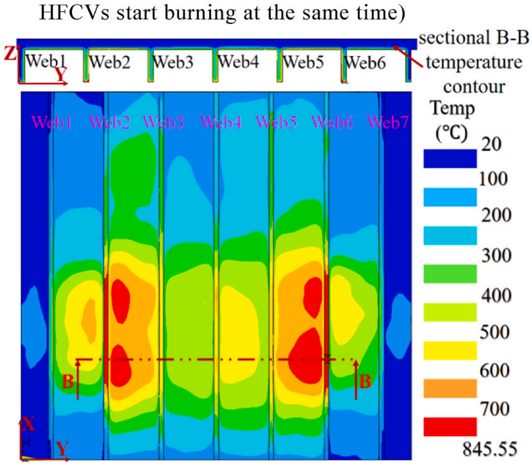

(b-2) Concrete temperature in ANSYS at 3300s in scenario 6 (fire spread to the adjacent HFCVs after 20 min)

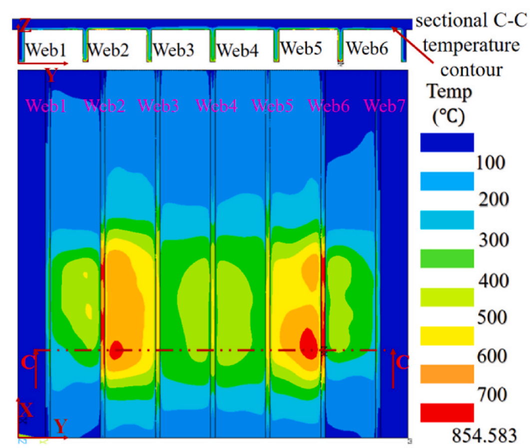

(b-3) Concrete temperature in ANSYS at 3900s in scenario 7 (fire spread to the adjacent HFCVs after 30 min)

Fig. 9. Visualization of instantaneous flame with gas temperature in FDS at 1122.2s, and maximum temperature contours of concrete surface and ceiling cross-section in ANSYS under different fire spread times and 2 mm TPRD nozzle.

while the maximum temperature at depth h = 0.6 m is about 200 °C.

Concrete temperatures along ceiling depth and concrete strength reduction factors in hot and cold conditions are displayed in Figs. 11(a) and (b), respectively. Temperatures in Fig. 11(a) are extracted at the time that the maximum temperature appears in 0.05 m depth of web4. For example, temperatures of 0 min, 20 min, and 30 min fire spread scenarios are obtained at 4800 s, 5100 s, and 5100 s, separately. At these times, the concrete compressive strength of web4 in the HFCV fire decreases up to a maximum value of 0.83 times the original strength. However, the concrete compressive strength of the part of the flange above web4 is almost close to the strength at normal temperature. This illustrates that webs of the concrete ceiling need to be maintained after HFCV fires. In Fig. 11(b), the maximum concrete temperatures at the same depths are not affected by the fire spread times. The residual compressive strength of web4 is 0.7–0.85 times the residual strength in the ambient temperature in the upper part of the web (h = 0.05 m–0.6 m). The bottom surface of the web is subjected to much higher temperatures and hence very significant damage to the concrete, where the residual strength decreases to 0.02 times the original residual strength. However, this happens in the tensile zone of the concrete, where the reinforcing bars can still take the tensile forces and maintain a good load-bearing capacity of the slabby in a limited depth in the HFCVs fire.

6. Discussion

This study examines the thermal behaviors of concrete structures subjected to HFCV fires in a car park setting. The simulation results presented in section 5 highlight the significance of the TPRD nozzle diameter. Specifically, larger nozzle diameters are associated with increased maximum HRR values and higher maximum concrete surface temperatures. Additionally, the TPRD nozzle diameter impacts the concrete strength, affecting both compressive strength and residual compressive strength. In scenarios involving multiple HFCVs, both the maximum HRR values and maximum concrete surface temperatures surpass those observed in single HFCV car park fires. The time when the concrete surface temperature reaches the peak value also varies depending on the spread of the fire between vehicles.

The car park fire model used in this study is constructed in a straightforward manner and validated using several sub-models due to limited test data. For instance, the HFCV main body fire is represented by HRR per unit area, and the car park structure is analyzed locally. This methodology is also available for studying other large and complex fire scenarios.

Investigating the concrete temperature in HFCV fires is crucial for improving fire safety measures and for developing robust post-fire assessment strategies in practical engineering applications. However, the influence of fire spread time on the concrete thermal response is not significant within the selected range, whereas the TPRD diameter has a

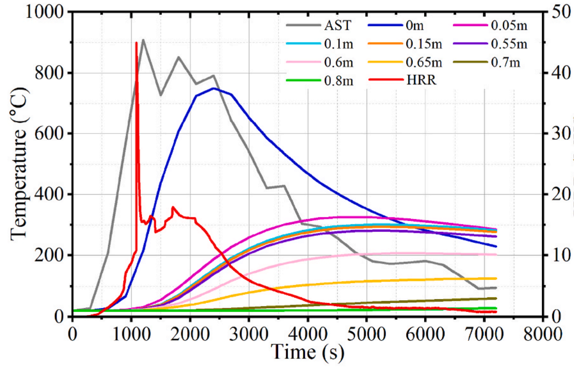

(a) Three HFCVs start burning at the same time (scenario 5)

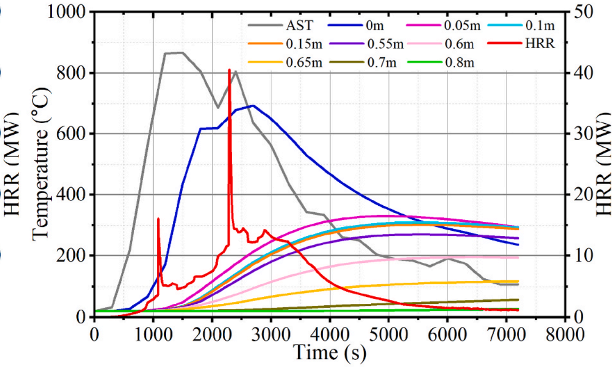

(b) Two side HFCVs start burning after 20 min (scenario 6)

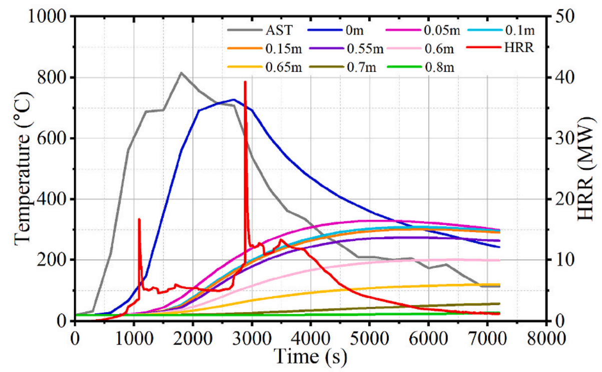

(c) Two side HFCVs start burning after 30 min (scenario 5)

Fig. 10. Concrete temperature and HRR histories under different fire spread times and concrete depth h (X = 3.85 m, Y = 4.25 m).

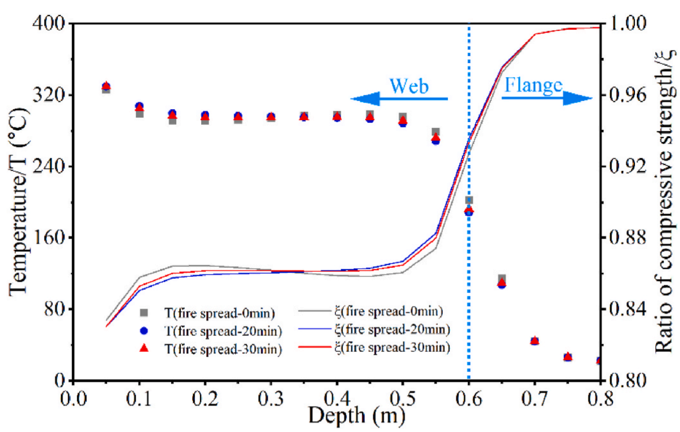

(a)

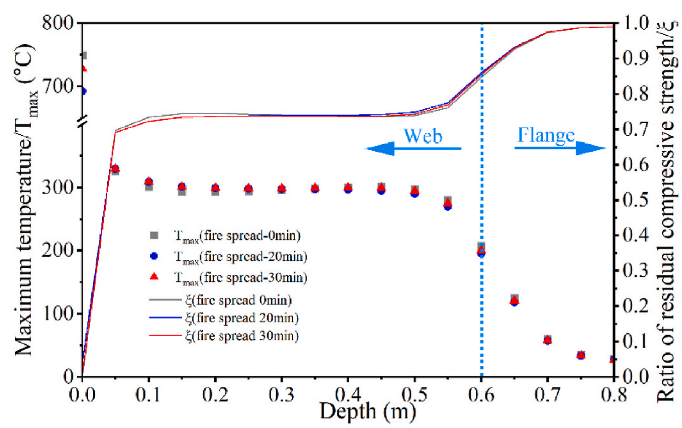

(b)

Fig. 11. Concrete temperatures and ratios of concrete strength in a fire along concrete depth h under different fire spread times (x = 3.85 m, y = 4.25 m): (a) hot condition (b) cold condition.

substantial impact.

Therefore, it is necessary to incorporate additional parameters in the study of HFCV fires. To enhance the realism of the numerical model, more detailed considerations of the HFCV fire model should be included, and the use of a two-way coupling method should be considered.

7. Conclusions

In this study, the thermal response of a concrete ceiling slab of a semi-open car park exposed to HFCV fire scenarios is analyzed employing an automatic one-way coupled CFD-FEA methodology. CFD and FEA simulations are conducted in FDS and ANSYS Mechanical APDL, respectively. In the coupling process, a one-way coupling interface called FDS2FTMI is used to transfer data from FDS to ANSYS. The coupling process is validated by comparing concrete temperatures predicted in a simulation with those registered in an experiment described in the literature, where an RC beam has been exposed to a standard fire in a propane furnace. The HFCV fire, assumed to consist of a vehicle main body fire and hydrogen jet fire, is studied in this paper. A total of seven HFCV fire scenarios, including four TPRD nozzle diameters (1 mm, 2 mm, 3 mm, and 4 mm) and three fire spread times among three HFCVs (0 min, 20 min, and 30 min), are simulated to investigate the HRR, concrete temperatures, and concrete strength. The main results are as follows.

(1) The maximum HRR value increases with a larger value of TPRD nozzle diameter, while it decreases with an increment of the fire spread time from the central vehicle to the adjoining ones. TPRD nozzle activation can result in a striking sudden peak value of HRR, and several peak values of HRR could happen in a fire as the TPRD nozzle activates at different times.
(2) The maximum concrete temperature (at the surface and inside the web) increases with the TPRD nozzle diameter. Consistently, for higher TPRD, the damage of the concrete also increases, as the residual strength degradation is higher when the maximum temperature reached by the concrete during the fire is higher.
(3) Instead, the fire spread time between HFCVs does not significantly affect the maximum concrete temperatures, although the time at which the maximum concrete temperatures are reached at a given depth increases with the increment in the fire spread time.

This study addresses one of the essential knowledge gaps in the field of HFCV fire safety science and engineering by developing a predictive model for car park fires involving HFCVs. The proposed technology is recommended for HFCV fire safety engineering to offer valuable insights into the safety design of systems and infrastructure associated with HFCV fires.

CRediT authorship contribution statement

Wenqian Liu: Conceptualization, Data curation, Formal analysis, Investigation, Methodology, Software, Validation, Writing – original draft, Funding acquisition. **Frank Markert:** Funding acquisition, Project administration, Supervision, Writing – review & editing. **Simo Hostikka:** Funding acquisition, Supervision, Writing – review & editing. **Luisa Giuliani:** Funding acquisition, Supervision, Writing – review & editing.

Declaration of competing interest

The authors declare that they have no known competing financial interests or personal relationships that could have appeared to influence the work reported in this paper.

Acknowledgments

The authors gratefully acknowledge the financial support provided by the Fuel Cells and Hydrogen 2 Joint Undertaking (now Clean Hydrogen Partnership) under Hy-tunnel CS Project [grant numbers 826193]. The authors gratefully acknowledge the support from the European Union's Horizon 2020 Research and Innovation program, Hydrogen Europe and Hydrogen Europe Research, the Finnish Fire Protection Fund (Palosuojelurahasto) [grant numbers VN/14165/2021], as well as Otto Mønsteds Fondand the Nordic Alliance funding for the PhD project by DTU.

References

[1] Meraner M. Car park fire: a review of fire incidents, progress in research and future challenges. The 7th international conference on fire in vehicles, Stavanger, Norway. April 24-25, 2023.
[2] Parry L. Luton airport fire car park to be 'fully demolished'. BBC News 3 Nov 2023. https://www.bbc.com/news/uk-england-beds-bucks-herts-67313813. [Accessed 1 January 2024].
[3] Holderith P. It's been exactly one year since the Felicity Ace caught fire with nearly 4000 cars onboard. THE DIREVE; 2023. https://www.thedrive.com/news/its-been-exactly-one-year-since-the-felicity-ace-caught-fire-with-nearly-4000-cars-onboard. [Accessed 1 January 2024].
[4] The Maritime Executive. Salvage of fire-damaged fremantle highway car carrier moves to Rotterdam. https://maritime-executive.com/article/salvage-of-fire-damaged-fremantle-highway-car-carrier-moves-to-rotterdam. [Accessed 1 January 2024].
[5] Molkov V, Kashkarov S, Makarov D, Fletcher J, Rattigan W. Explosion free in fire sel-venting (TPRD-less) type IV tanks: validation under extreme impinging 70MPa hydrogen jet fire conditions. Int J Hydrogen Energy 2023;48(100):40117–26. https://doi.org/10.1016/j.ijhydene.2023.09.020.
[6] Annerel E, Taerwe L, Merci B, Jansen D, Bamonte P, Felicetti R. Thermo-mechanical analysis of an underground car park structure exposed to fire. Fire Saf J 2013;57:96–106. https://doi.org/10.1016/j.firesaf.2012.07.006.
[7] Woo D, Seo JK. Numerical validation of the two-way fluid-structure interaction method for non-linear structural analysis under fire conditions. J Mater Sci Eng 2021;9(4):400. https://doi.org/10.3390/jmse9040400.
[8] Janardhan RK, Shakil S, Lu W, Hostikka S, Puttonen J. Coupled CFD-FE analysis of a long-span truss beam exposed to spreading fires. Eng Struct 2022;259:114150. https://doi.org/10.1016/j.engstruct.2022.114150.
[9] Feenstra JA, Hofmeyer H, Van Herpen RAP, Mahendran M. Automated two-way coupling of CFD fire simulations to thermomechanical FE analyses at the overall structural level. Fire Saf J 2018;96:165–75. https://doi.org/10.1016/j.firesaf.2017.11.007.
[10] Dellepiani MG, Munoz GR, Yanez SJ, Guzmán CF, Flores EIS, Pina JC. Numerical study of the thermo-mechanical behavior of steel–timber structures exposed to fire. J Build Eng 2023;65:105758. https://doi.org/10.1016/j.jobe.2022.105758.
[11] Prasad K, Baum HR. Coupled fire dynamics and thermal response of complex building structures. Proc Combust Inst 2005;30(2):2255–62. https://doi.org/10.1016/j.proci.2004.08.118.
[12] Tondini N, Vassart O, Franssen J. Development of an interface between CFD and FE software. 7th Int. Conf. Struct. Fire 2012:459–68. https://hdl.handle.net/2268/128362.
[13] Silva JCG, Landesmann A, Ribeiro FLB. Fire-thermomechanical interface model for performance-based analysis of structures exposed to fire. Fire Saf J 2016;83:66–78. https://doi.org/10.1016/j.firesaf.2016.04.007.
[14] Wickstrom U. Heat transfer by radiation and convection in fire testing. Fire Mater 2004;28(5):355–415. https://doi.org/10.1002/fam.839.
[15] de Boer JGGM, Hofmeyer H, Maljaars J, van Herpen RAP. Two-way coupled CFD fire and thermomechanical FE analysis of a self-supporting sandwich panel façade system. Fire Saf J 2019;105:154–68. https://doi.org/10.1016/j.firesaf.2019.02.011.
[16] Alos-Moya J, Paya-Zaforteza I, Garlock MEM, Loma-Ossorio E, Schiffner D, Hospitaler A. Analysis of a bridge failure due to fire using computational fluid dynamics and finite element models. Eng Struct 2014;68:96–110. https://doi.org/10.1016/j.engstruct.2014.02.022.
[17] Silva JCG, Landesmann A, Ribeiro FLB. Performance-based analysis of cylindrical steel containment Vessels exposed to fire. Fire Saf J 2014;69:126–35. https://doi.org/10.1016/j.firesaf.2014.08.013.
[18] Tondini N, Morbioli A, Vassart O, Lechêne S, Franssen J-M. An integrated modelling strategy between a CFD and an FE software: methodology and application to compartment fires. J Struct Fire Eng 2016;7(3):217–33. https://doi.org/10.1108/JSFE-09-2016-015.
[19] Yan X, Charlier M, Gernay T. Thermal response of steel framing members in open car park fires. Front Struct Civ Eng 2022;16(9):1071–88. https://doi.org/10.1007/s11709-022-0879-0.
[20] Lin H, Luan H, Yang L, Han C, Karampour H, Chen G. Asafety assessment methodology for thermo-mechanical response of offshore jacket platform under fire. Process Saf Environ Protect 2022;160:184–98. https://doi.org/10.1016/j.psep.2022.02.007.
[21] Welch S, Miles S, Kumar S, Lemaire T, Chan A. FIRESTRUC – integrating advanced three-dimensional modelling methodologies for predicting thermo-mechanical behavior of steel and composite structures subjected to natural fires. Fire Saf Sci 2009;9:1315–26. https://doi:10.3801/IAFSS.FSS.9-1315.
[22] McGrattan K, McDermott R, Vanella M, Hostikka S, Floyd J. Fire Dynamics simulator user's guide. 1019 sixth ed. NIST Special Publication; 2022. https://doi.org/10.6028/NIST.SP.1019. . [Accessed 3 March 2024] (web: FDS-SMV Manuals (nist.gov)).
[23] Yan X, Gerny T. Numerical modeling of localized fire exposures on structures using FDS-FEM and simple models. Eng Struct 2021;246(1):112997. https://doi.org/10.1016/j.engstruct.2021.112997.
[24] Wickstrom U, Duthinh D, McGrattan K. Adiabatic surface temperature for calculating heat transfer to fire exposed structures. In: Proc. Elev. Int. Interflam conf. Intersci. Commun. London; 2007.
[25] Silva JCG. FDS2FTMI User's Guide: an automated code to one-way coupling between FDS and FEM using FTMI. https://github.com/firemodels/fds/blob/master/Utilities/Structural_Interaction/fds2ftmi/scripts/build_fds2ftmi.sh. [Accessed 3 March 2024].
[26] ANSYS. Mechanical APDL theory reference. Canonsburg, PA: ANSYS Inc; 2015., Version 16.2.
[27] Kumar P, Kodur VKR. Effect of fire-induced restraint forces on fire behavior of reinforced and prestressed concrete beams. Eng Struct 2023;207:115200. https://doi.org/10.1016/j.engstruct.2022.115200.
[28] Zhang C, Silva JCG, Weinschenk C, Kamikawa D, Hasemi Y. Simulation methodology for coupled fire-structure analysis: modeling localized fire tests on a steel column. Fire Technol 2016;52:239–62. https://doi.org/10.1007/s10694-015-0495-9.
[29] EN 1992-1-2. Eurocode 2: design of concrete structures-Part 1-2: general rules-Structural fire design. 2004. p. 26–9.
[30] EN 1993-1-2. Eurocode 3: design of steel structures-Part 1-2: general rules-Structural fire design. 2005. p. 25–6.
[31] Ahmed A. Behavior of FRP-Strengthened reinforced concrete beams under fire conditions. Michigan State University; 2010. p. 67–99. Doctoral thesis.

[32] Søgaard D. Fire spread from hydrogen-fueled vehicles to adjacent vehicles in open car parks. Mater thesis, department of civil engineering. Denmark: Technical University of Denmark; 2018. p. 23–35.
[33] Nexo fuel cell vehicle overview. 2023. https://www.hyundaiusa.com/us/en/vehicles/nexo. [Accessed 1 January 2024].
[34] Kang S, Lee KM, Kwon M, Lim OK, Choi JY. A quantitative analysis of the fire hazard generated from hydrogen fuel cell electric vehicles. International Journal of Fire Science and Engineering 2022;36(2):26–39. https://doi.org/10.7731/KIFSE.f4b33457.
[35] E-laboratory. https://elab.hysafer.ulster.ac.uk/. [Accessed 1 January 2024].
[36] Liu W, Markert F, Giuliani L, Hostikka S. Analyzing the gas temperature of a hydrogen jet fire in a compartment with the Fire Dynamics Simulator. Int J Hydrogen Energy 2024;53:1097–106. https://doi.org/10.1016/j.ijhydene.2023.11.306.
[37] Tamura Y, Takabayashi M, Takeuchi M. The spread of fire from adjoining vehicles to a hydrogen fuel cell vehicle. Int J Hydrogen Energy 2014;39(11):6169–75. https://doi.org/10.1016/j.ijhydene.2014.01.140.
[38] Hertz KD. Design of fire-resistant concrete structures. ICE Publishing; 2019. https://doi.org/10.1680/dofrcs.64447.001 [chapter 2]: Materials.
[39] Özgür Atayılmaz Ş. Transient and steady-state natural convection heat transfer from a heated horizontal concrete cylinder. Int J Therm Sci 2010;49(10):1933–43. https://doi.org/10.1016/j.ijthermalsci.2010.05.019.
[40] Liu W, Riba Clasca FG, Markert F, Giuliani L. Fire spread scenarios involving hydrogen vehicles. The 9th international conference on hydrogen safety. Scotland: Edinburgh; September .